Article

A universal interface for plug-and-play assembly of stretchable devices

Check for updates

Ying Jiang[1], Shaobo Ji[1], Jing Sun[2], Jianping Huang[2], Yuanheng Li[2], Guijin Zou[3], Teddy Salim[1], Changxian Wang[1], Wenlong Li[4], Haoran Jin[1], Jie Xu[5], Sihong Wang[5], Ting Lei[5], Xuzhou Yan[5], Wendy Yen Xian Peh[6], Shih-Cheng Yen[6], Zhihua Liu[4], Mei Yu[2], Hang Zhao[2], Zechao Lu[2], Guanglin Li[2], Huajian Gao[3,7], Zhiyuan Liu[2✉], Zhenan Bao[5✉] & Xiaodong Chen[1,4,8✉]

Stretchable hybrid devices have enabled high-fidelity implantable[1–3] and on-skin[4–6] monitoring of physiological signals. These devices typically contain soft modules that match the mechanical requirements in humans[7,8] and soft robots[9,10], rigid modules containing Si-based microelectronics[11,12] and protective encapsulation modules[13,14]. To make such a system mechanically compliant, the interconnects between the modules need to tolerate stress concentration that may limit their stretching and ultimately cause debonding failure[15–17]. Here, we report a universal interface that can reliably connect soft, rigid and encapsulation modules together to form robust and highly stretchable devices in a plug-and-play manner. The interface, consisting of interpenetrating polymer and metal nanostructures, connects modules by simply pressing without using pastes. Its formation is depicted by a biphasic network growth model. Soft–soft modules joined by this interface achieved 600% and 180% mechanical and electrical stretchability, respectively. Soft and rigid modules can also be electrically connected using the above interface. Encapsulation on soft modules with this interface is strongly adhesive with an interfacial toughness of 0.24 N mm⁻¹. As a proof of concept, we use this interface to assemble stretchable devices for in vivo neuromodulation and on-skin electromyography, with high signal quality and mechanical resistance. We expect such a plug-and-play interface to simplify and accelerate the development of on-skin and implantable stretchable devices.

Stretchable hybrid devices are assembled by connecting several modules together (Fig. 1a). They can be classified as three elementary types: soft modules that mechanically match tissue/skin of humans or soft robots, rigid modules comprising Si-based microelectronics and encapsulation modules for protection. These modules, with different materials, form factors and processing techniques, are typically manufactured independently and assembled thereafter using commercial conductive pastes such as anisotropic conductive film (ACF)[18–20] and silver paste[21–23]. The challenge is that the assembled connections suffer from interfacial failure under deformation due to the mechanical mismatches between the pastes and modules (Extended Data Fig. 1a–d). This issue greatly limits the complexity and robustness of stretchable electronic systems.

Various approaches have been attempted to resolve these issues. All-soft electronics (without rigid Si components) have been developed to eliminate mechanical mismatch at interfaces[16,24,25]. However, Si-based components are still necessary for signal processing and wireless communications. Others have substituted rigid pastes with liquid metal[26–28], but its high surface tension results in low interfacial adhesion

and it may smear to undesirable places. Composites consisting of a self-healing polymer or hydrogel matrix with conductive fillers potentially eliminates[29–31] or substitutes[32] the use of pastes. However, their large thickness (tens to hundreds of micrometres) leads to mechanical mismatch and reduced mechanical or electrical robustness, as well as inapplicability to ultrathin electronics.

In this work, we created a biphasic, nano-dispersed (BIND) interface that can reliably connect soft, rigid and encapsulation modules together, in a plug-and-play way without the use of pastes (Fig. 1b). Any modules bearing the BIND interface can simply be pressed together face-to-face to form BIND connections in less than 10 s (Fig. 1c). We prepared the BIND interface by thermally evaporating gold (Au) or silver (Ag) nanoparticles to form interpenetrating nanostructure inside a self-adhesive styrene-ethylene-butylene-styrene (SEBS) thermoplastic elastomer, which is a soft substrate widely used in stretchable electronics. Nanoparticles near the surface of the SEBS matrix form a biphasic layer (roughly 90 nm deep), in which some nanoparticles are totally immersed whereas others are partly exposed (Fig. 1b inset). This interfacial structure produced exposed SEBS and Au on the surface and
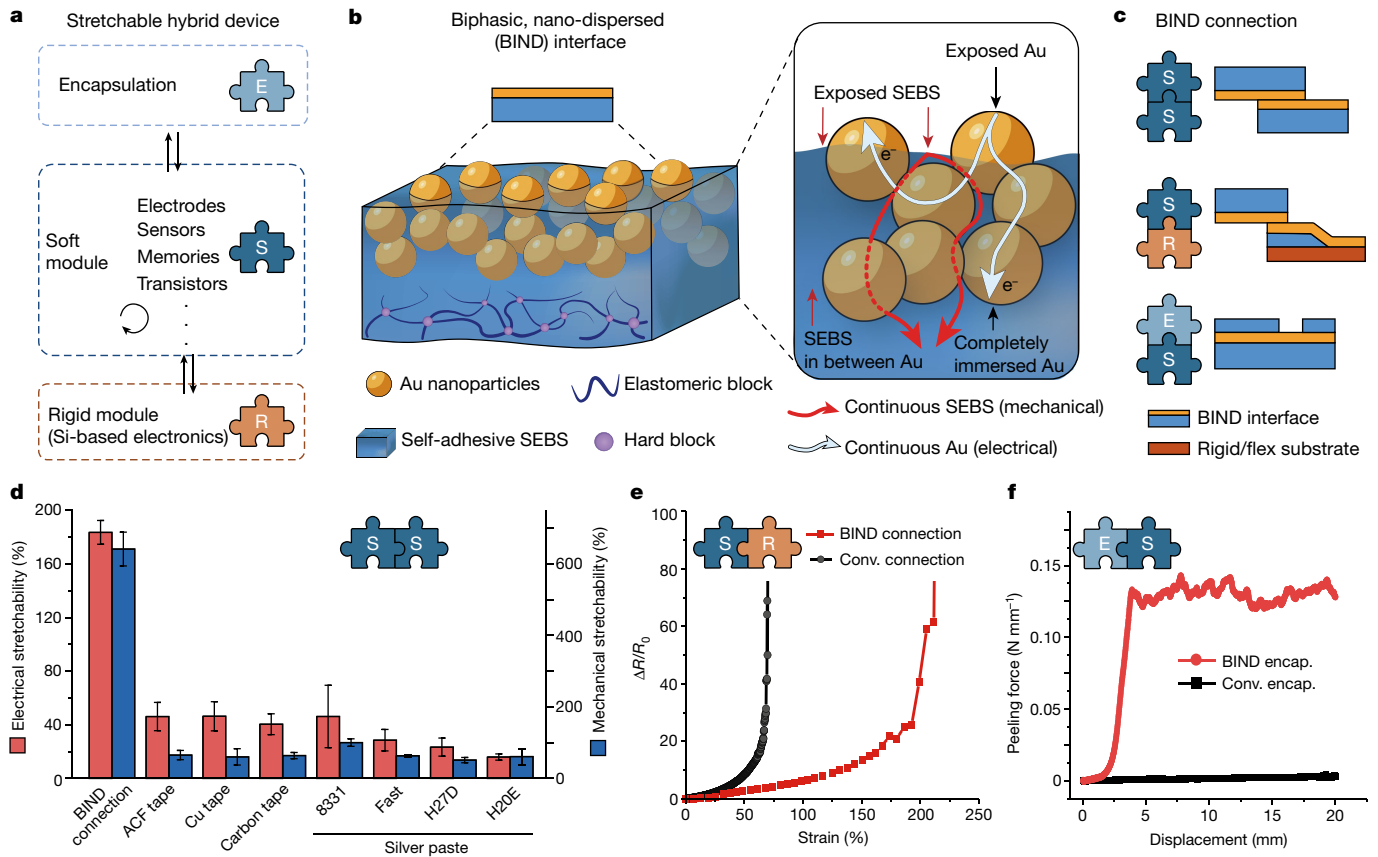
Fig. 1 | BIND connection for stretchable hybrid device. a, The schematic shows stretchable hybrid devices are typically assembled from three elementary modules (encapsulation, soft and rigid modules), through modular interfaces. **b**, Illustration of a BIND interface. Magnified illustration (right) shows exposed SEBS and Au, whereas the interpenetrating nanostructure provides a continuous mechanical and electrical pathway. **c**, The BIND connection between different modules. Soft–soft connects two BIND interfaces. Soft–rigid involves one BIND interface connected to another BIND interface fabricated on a rigid/flexible substrate. In soft–encapsulation, the encapsulation material pressed onto a BIND interface can be patterned to expose parts of the BIND interface. **d**, Compared to commercial pastes, soft–soft BIND connection (overlapping area

5 mm width × 10 mm length) showed greater electrical (180%) and mechanical (600%) stretchability. Error bars are s.d. from 4–5 samples. **e**, Soft–rigid BIND connection obtained by pressing one BIND interface with another BIND interface fabricated on PI substrate showing electrical stretchability of 200% (versus roughly 67% for conventional (conv.) connection using commercial ACF tape to connect soft PDMS with PI). **f**, Soft–encapsulation BIND connection, which involves pressing an SEBS encapsulation layer (roughly 100 μm thick) onto a BIND interface, showing a larger peeling force plateau (0.12 N mm^{-1}) than a conventional connection formed by PDMS encapsulation on a PDMS–Au interface (0.002 N mm^{-1}).

interpenetrating Au nanoparticles inside the matrix, which provides both continuous mechanical and electrical pathways for robust BIND connections.

Electro-mechanical performance

To begin, we tested a soft–soft BIND connection by pressing two BIND interfaces together. As a control, we connected polydimethylsiloxane (PDMS)–Au substrates using commercial pastes such as ACF tape, copper (Cu) tape, carbon tape and four types of silver paste. Compared with commercial pastes, BIND connections showed nearly three times greater electrical stretchability (maximum strain before electrical breaking, >180% versus roughly 45%) and nearly ten times greater mechanical stretchability (maximum strain before mechanical breaking, >600% versus roughly 60%) (Fig. 1d and Extended Data Fig. 1e–i). Further, BIND connections showed less than four times change in relative resistance at 50% strain. Finite element analysis-assisted mechanical analysis showed that the attenuated strain concentration in BIND connection contributes to its high electrical stretchability (Supplementary Note 1 and Supplementary Fig. 1). Such robust BIND connections require a balanced ratio between SEBS and the metallic nanoparticles, which is controlled by the nanoparticle deposition rate (0.5–1.0 Å s^{-1})

and thickness (45–60 nm) (Extended Data Fig. 2). Larger deposition rates and thicknesses result in a non-adhesive interface whereas smaller ones render the interface non-conductive.

The plug-and-play BIND connections are very easy to form and use by simply finger pressing for less than 10 s. This is because the pressing time, pressure and peeling direction (lap shear or 90° peeling) have little influence on the adhesion strength of the connections (Extended Data Fig. 3a–c). The BIND connections with a cut can still be stretched to 500%, demonstrating antitearing qualities (Extended Data Fig. 3d–g). Because BIND connections do not require paste, they are well suited to high-resolution patterning (Extended Data Fig. 4a,b). Depending on the application, the choice of nanoparticles can be expanded to Ag/Ag or Ag/Au BIND connections (Extended Data Fig. 4c).

We further formed soft–rigid BIND connections by pressing a soft BIND interface to another BIND interface fabricated on rigid or flexible substrates, including polyimide (PI), polyethylene terephthalate (PET), glass and metal (Extended Data Fig. 4d). Because these rigid/flexible substrates are compatible with printed circuit board (PCB) manufacturing, the corresponding rigid/flexible modules can fully use the processing capability of Si-based microelectronics. Similar to the soft–soft connection, soft–rigid BIND connections also showed a lower change in relative resistance (Fig. 1e), higher electrical (200%) and
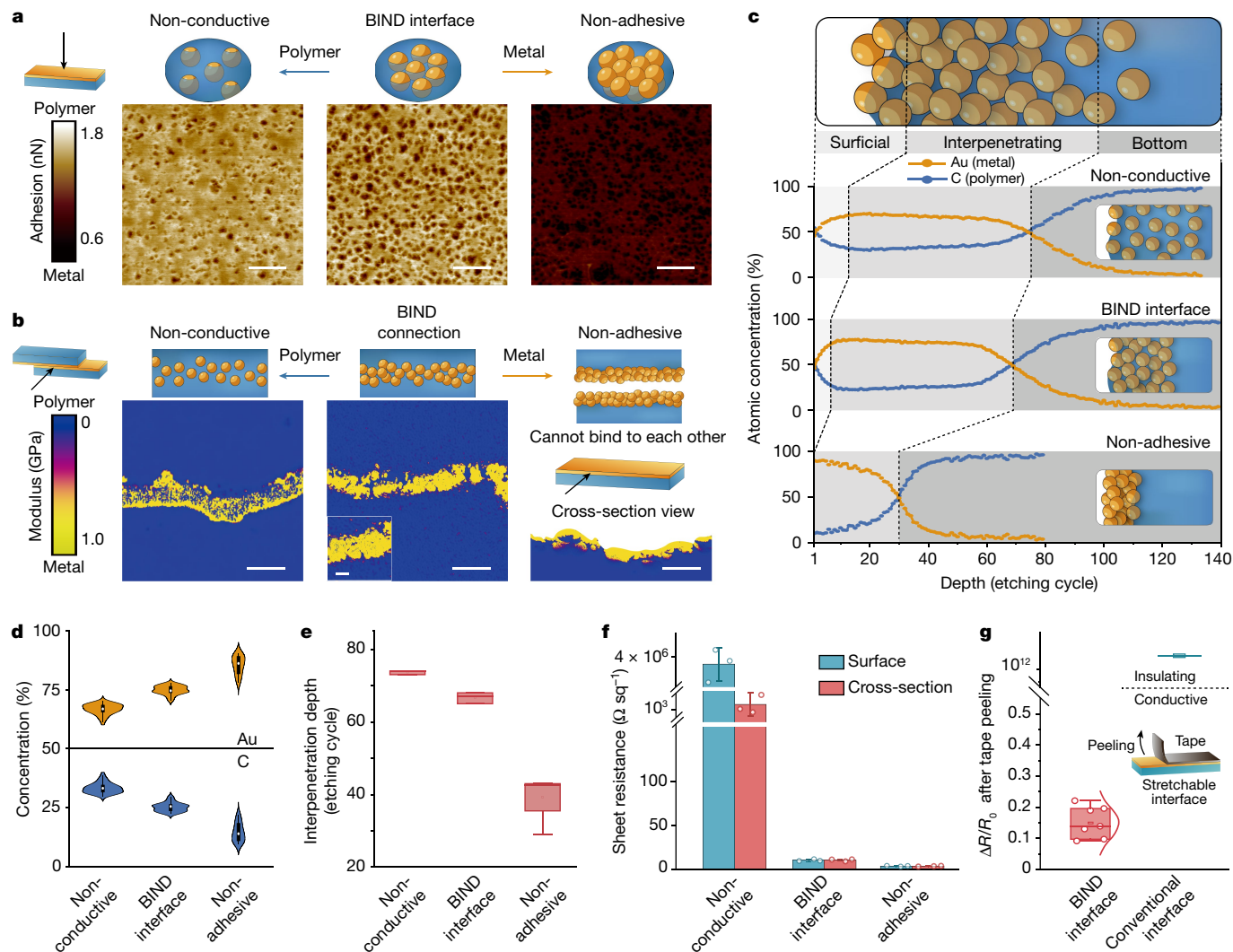
Fig. 2 | Structural analysis of BIND interface and connection. a, Adhesion AFM mapping shows the surface of BIND interface (middle) has both exposed polymer (light brown) and metal (dark brown) phases. The non-conductive interface (left) has a high polymer to metal ratio on its surface, whereas the non-adhesive interface (right) has a low ratio. Scale bar, 100 nm. **b**, Modulus AFM mapping shows decreasing polymer to metal ratio, from non-conductive interfaces (left), to BIND interfaces (middle and magnified view in inset) and to non-adhesive interfaces (right). Scale bar, 400 nm; inset scale bar, 100 nm. **c**, Schematic (top) of the surficial, interpenetrating and bottom layers of the interface and the corresponding atomic concentration from AES (bottom) show Au nanoparticles are distributed as interpenetrating network.

Au nanoparticles in the non-conductive interface are sparsely distributed whereas those in the non-adhesive interface are densely packed at the surface. **d,e**, Auger depth profiling shows the interpenetrating layer of the BIND interface is 75% Au and 25% C (**d**), with an Au penetration depth of roughly 70 etching cycles (**e**). **f**, Surficial and cross-sectional sheet resistance are consistent with polymer to metal ratio for all interfaces. **g**, Unlike the conventional PDMS–Au interface, the BIND interface withstands scotch tape peeling as shown by its lower change in resistance. Violin plot in **d**, box plots in **e,g** are from 3–7 samples (middle line/hollow point, median; box limits, upper and lower quartiles and whiskers, 1.5× interquartile range). Error bars in **f** are s.d. from three samples.

mechanical (800%) stretchability than connections with commercial conductive pastes (Extended Data Fig. 4e). Both soft–rigid and soft–soft BIND connections demonstrate cyclic durability for 600 cycles under tensile, bending and twisting loading, whereas mechanical stretchability was basically unchanged afterwards (Supplementary Fig. 2). In addition, the soft–rigid BIND connection can be used to assemble surface mount devices such as LEDs (Supplementary Fig. 3).

Our BIND interface can also connect encapsulation modules strongly. The soft–encapsulation BIND connections, fabricated by pressing an SEBS encapsulation layer on a BIND interface, were subjected to a 180° peeling test (Fig. 1f). Interfacial toughness was defined as twice the peeling force plateau divided by the sample width[33]. Because the surface-exposed polymer on the BIND interface provides binding areas for the encapsulation layer, its interfacial toughness (0.24 N mm^{-1}) is 60 times larger than a conventional encapsulation (PDMS or other

encapsulation layer bonded on a PDMS–Au interface) (Extended Data Fig. 4f). Further, the encapsulated BIND interface can be selectively patterned to expose specific parts for applications such as electrophysiology electrode pads (Methods and Extended Data Fig. 4g). Besides, the resolution of single BIND interface, BIND connection and BIND encapsulation can all achieve 0.1 mm line width (Extended Data Fig. 4h–j).

Structural analysis

To understand the plug-and-play nature of the BIND interface, we investigated its surface and inner structures at nanoscale. Adhesion atomic force microscopy (AFM) mapping shows exposed polymer and metal phases on the surface of the BIND interface (middle panel in Fig. 2a). Both phases were clearly distinguishable because polymers bind more strongly to the AFM tip than metals. From adhesion, height

and modulus AFM mapping, we found that the ratio of polymer to metal phase affects the macroscopic electrical and mechanical properties of the interfaces. An excess of the polymer phase results in a highly adhesive but non-conductive interface, whereas the lack of it makes the interface non-adhesive (left and right panels in Fig. 2a and Extended Data Fig. 5). On a BIND interface, the ratio of exposed polymer to metal is optimal: exposed self-adhesive SEBS provides the mechanical strength of the BIND connection due to the partial polymer welding[34–36] involving the interdiffusion of ethylene-butylene segments; exposed metal provides Ohmic contact and thus the electrical conductivity of the BIND connection. Further cross-sectional AFM mapping shows BIND connection contains a nano-scaled interpenetrating network of polymer and metal, with a depth of roughly 90 nm under the surface of each interface (middle panel in Fig. 2b and Extended Data Fig. 6a,b, f–h). Similar to what was observed on the surface, the non-conductive connection also contained a large proportion of polymer phase and showed lower conductivity than the BIND connection (left panel in Fig. 2b and Extended Data Fig. 6c–e). The non-adhesive interface, which failed to connect, had a concentrated metal phase on its surface (right panel in Fig. 2b and Extended Data Fig. 6i–k).

We further used Auger electron spectroscopy (AES) to profile the polymer and metal phases inside the interfaces at each etched layer (Fig. 2c and Supplementary Note 2, Supplementary Fig. 4). The non-conductive interface had a deep and sparse distribution of Au nanoparticles, whereas the non-adhesive interface had a densely stacked layer of Au and almost no polymer on its surface. In comparison, the surface layer of our BIND interface contained polymer (50% C) and metal (50% Au), which gradually changed to 75% Au and 25% C (Fig. 2d), and ended at roughly 70 etching cycles (Fig. 2e). Such a bicontinuous pathway of polymer and metal determines the macroscopic electrical resistance of the BIND interface. Although the metallic phase in the BIND interface is deeper than the non-adhesive interface, both interfaces showed similar surficial and cross-sectional sheet resistance of less than $10 \, \Omega \, \text{sq}^{-1}$ (Fig. 2f). Furthermore, the biphasic interpenetrating structure allows the BIND interface to resist tape peeling, whereas the conventional PDMS–Au interface is easily rendered non-conductive (Fig. 2g and Supplementary Fig. 5).

Although exposed SEBS inside microcracks on BIND interface could be another source of mechanical adhesion, we removed this possibility by scanning electron microscopy (SEM) and AFM studies of the non-conductive, BIND and non-adhesive interfaces under 0, 50 and 100% strains (Supplementary Note 3). Despite having longer and wider microcracks that could expose more SEBS for adhesion, the non-adhesive interface was less adhesive than the non-conductive interface that had smaller and narrower microcracks (Supplementary Fig. 6). Together, our results show that the adhesion and conductivity of our BIND connection can only originate from its unique interpenetrating nanostructure.

Furthermore, we proposed a biphasic network growth model to depict the nanomechanics process in the BIND interface formation based on experimental data and molecular dynamics simulations (Supplementary Note 4 and Supplementary Fig. 7). Our growth model begins with a flux of high momentum Au atoms in the gas phase approaching the softened SEBS substrate. As the Au atoms bombard the softened SEBS, they penetrate and form independent nuclei below the SEBS surface. Over time, these independent Au nuclei grow in size and depth before eventually coalescing to form interpenetrating nanostructures in the BIND interface.

BIND device for in vivo neuromodulation

To demonstrate how practical BIND connections are for plug-and-play assembly of different modules, we used them to build stretchable devices for in vivo neuromodulation. Devices for such delicate tasks require an ultrathin, soft module that can wrap snugly around the nerve

(or muscle) and a thick, soft module for robust wiring. We built a BIND device by connecting an ultrathin conformal module to a thick wiring module through plug-and-play BIND connections where both modules were covered with a BIND encapsulation layer (Fig. 3a and Supplementary Fig. 8). For in vivo neuromodulation, the ultrathin end of the BIND electrode is slid under the nerve or muscle, folded over and pressed to secure the electrode before the supporting layer is removed (Fig. 3b). Because the BIND electrode is self-adhesive, no suturing is required.

Our BIND electrode is both conformable and strong. It wraps around different-sized tissues (ranging from centimetres to hundreds of nanometres), including the common peroneal nerve, sciatic nerve, peroneus longus muscle, cerebral cortex and bladder wall (Extended Data Fig. 7a–e). One-piece electrodes that were completely thick could not conformally wrap the muscle (or nerve), leaving large gaps that could cause signal loss, whereas completely ultrathin electrodes crumpled easily in the wiring region and induced interference (Fig. 3c). Whereas all three electrodes successfully detected subcutaneous compound muscle action potential (CMAP) from the peroneus longus muscle in a rat leg (Fig. 3d), the BIND electrode showed the lowest baseline noise and highest signal-to-noise (SNR) ratio (Fig. 3e). Recordings from the BIND electrode showed a consistent pattern of stimulation artefacts and evoked CMAP signals (Fig. 3f). Further, mechanical interference commonly encountered in vivo such as touching and tugging affected the performance of the BIND electrode very little (Extended Data Fig. 7f–i and Supplementary Video 1). The impedance of BIND interface was stable up to 70% strain and the BIND connection only contributed to the d.c. component in impedance (Extended Data Fig. 7j,k). These results demonstrate that devices that combine modules with different form factors (thickness), as in our BIND electrode, show remarkably enhanced signal quality.

Additionally, the modular BIND electrode is universally applicable. We applied one BIND electrode to stimulate the common peroneal nerve, and simultaneously used another BIND electrode to record the evoked subcutaneous CMAP from the peroneus longus muscle (Extended Data Fig. 8a,b and Supplementary Fig. 9). The recorded CMAP signal following current stimulation showed an increasing trend before reaching saturation (Fig. 3g, Extended Data Fig. 8c–f and Supplementary Video 2). Further, placing a four-channel BIND electrode on the rat cerebral cortex enabled electrocorticography (ECoG) recording (Extended Data Fig. 8g). The intimate contact between the ultrathin module and soft cortex provided high-quality ECoG signals, whereas that of epileptic rats had larger amplitudes and higher power in the ECoG frequency range than healthy rats (Fig. 3h, Extended Data Fig. 8h and Supplementary Video 3). We also used the BIND electrode for bladder stimulation, in which the BIND electrode transmitted electrical pulses to evoke bladder contraction resulting in urination measured by an external pressure sensor (Fig. 3i and Extended Data Fig. 8i–k).

Together, these experiments demonstrate that conformal contact and durable wiring of electrodes achieved through BIND connections enable delicate in vivo neuromodulation and obtain high-quality signals. This would not be possible with one-piece electrodes that crumple easily or wrap poorly around tissues.

BIND device for 21-channel on-skin electromyography

To demonstrate that plug-and-play BIND connections outperform their commercial pastes counterparts, we further assembled a 21-channel on-skin electromyography (EMG) BIND device from five modules: ultrathin conformal electrode, thick wiring, PI PCB and two encapsulation layers (Fig. 4a). All five modules were fabricated separately and integrated using BIND connections in a plug-and-play manner (Fig. 4b, Supplementary Fig. 10 and Supplementary Video 4). The ultrathin electrode with an airtight conformal contact with skin[37–39] is crucial for signal fidelity and spatial resolution. Signals collected by the ultrathin electrode are relayed to the customized PI PCB through the thick wiring
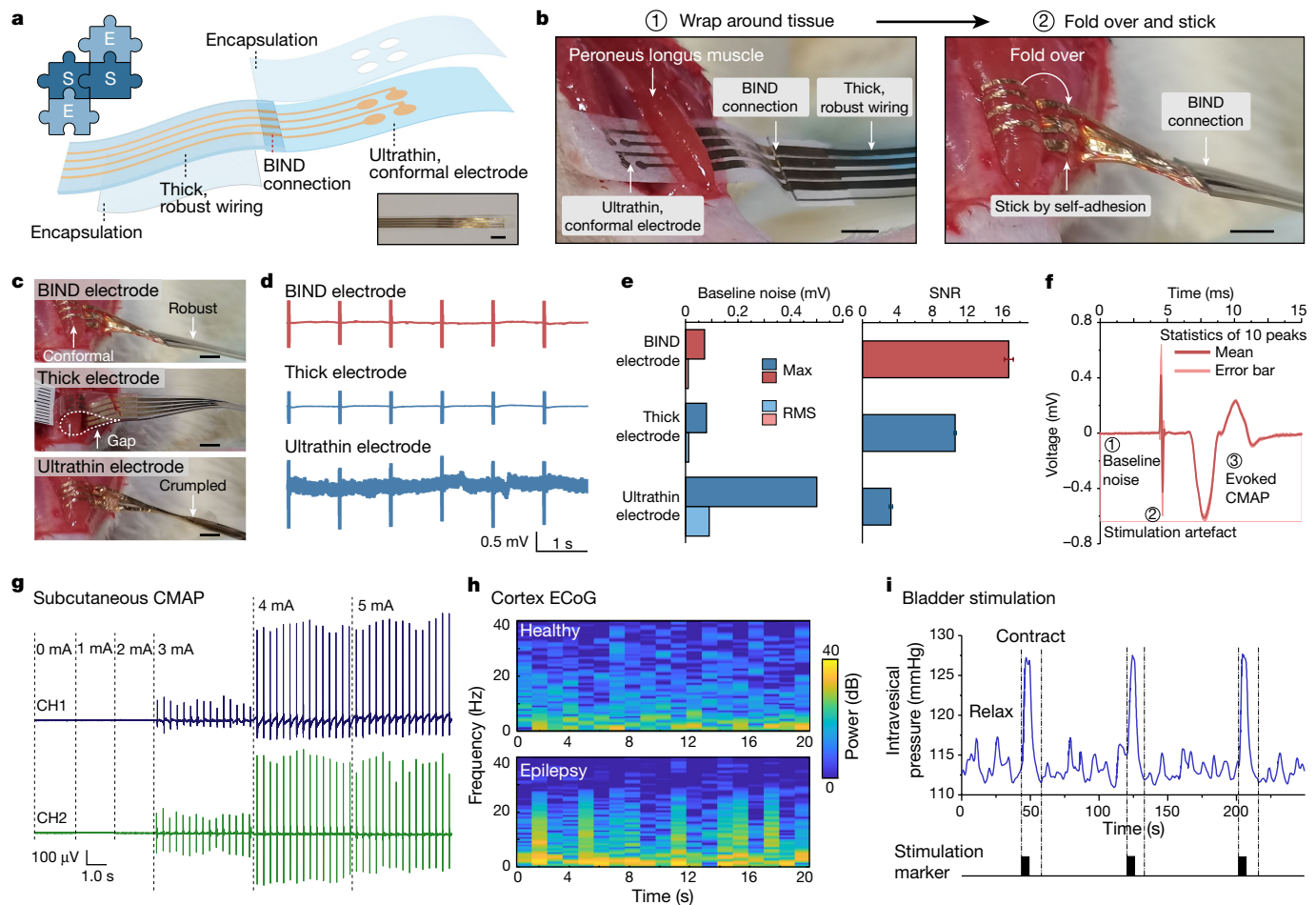
Fig. 3 | In vivo neuromodulation stretchable device assembled through plug-and-play BIND connections. a, Schematic of the BIND electrode device, consisting of an ultrathin, conformal electrode module, a thick wiring module and two encapsulation layers with exposure at contact areas. **b**, Applying BIND electrode onto the peroneus longus muscle involves sliding the electrode under the muscle and folding it over for adhesion. **c**, BIND electrode conformally wraps the tissue with robust wiring modules. The one-piece-thick electrode does not wrap snugly around the tissue and leaves gaps, whereas one-piece ultrathin electrode crumples easily. **d**, All three electrodes successfully recorded CMAP signals from the peroneus longus muscle in a rat leg, whose peroneal nerve was stimulated using a two-channel PI electrode. **e**, CMAP recordings from BIND electrode show the lowest baseline noise and highest SNR. RMS, root mean square. **f**, Recordings from BIND electrode consistently show a pattern of stimulation artefact and evoked CMAP. **g**, CMAP recordings from peroneus longus muscle obtained through a two-channel (CH1 and CH2) BIND electrode after the common peroneal nerve was stimulated using another BIND electrode. **h**, ECoG recording from an epileptic rat cortex has higher power in the ECoG frequency range than those from healthy rats. **i**, Bladder pressure increases when BIND electrode on the bladder wall stimulates the bladder muscle to contract and release urine. Error bars in **e**,**f** are s.d. from ten peaks. Scale bars are 1 cm in **a** and 5 mm in **b**,**c**.

module, and Si microelectronics in the PI PCB module conducted signal processing, storage and transmission. As a control, we connected conventional PDMS–Au electrodes in the same configuration using commercial ACF.

On-skin EMG electrodes typically experience mechanical interferences such as pressure or strain at the connection points. Such concentrated stress often leads to noisy signals and/or electrode failure. Our BIND electrode is resistant to such interferences. When pressure was applied on the connection with a tweezer clamp (Fig. 4c), signals from our BIND electrode remained clear while those from control ACF-connected electrode were weakened and noisy (Fig. 4d, Extended Data Fig. 9a,b and Supplementary Video 5). Specifically, the artefacts in BIND electrode were smaller than the control electrode, induced by pressing (0.03 versus 0.24 mV) or releasing (0.12 versus 0.80 mV) (Fig. 4e). Furthermore, the BIND electrode showed a high SNR of fist clenching before (20.9 dB), during (17.2 dB) and after (20.3 dB) pressing, demonstrating the electrode collects signals reliably under pressure and recovers well afterwards (Fig. 4f). By contrast, control

electrode with an initial SNR of 11.0 dB suffered enormous signal loss (−0.06 dB SNR) during pressing and incomplete recovery afterwards (7.56 dB SNR). Besides pressure, the BIND connection also withstood strains up to 50%. Compared to the control electrode, the BIND electrode showed lower stretching (0.18 versus 0.28 mV) and releasing (0.13 versus 0.55 mV) artefacts and higher SNR during (9.2 versus 0.3 dB) and after (18.4 versus 11.3 dB) stretching (Extended Data Fig. 9c–g and Supplementary Video 5).

Our 21-channel BIND electrode can map EMG signals of various gestures, including hand movements (clench, open, raise, bend), finger movements (stretching of individual fingers) and different levels of maximum voluntary contraction (Fig. 4g, Extended Data Fig. 10a and Supplementary Video 6). It also works well underwater with good resistance against mechanical interferences (Fig. 4h, Extended Data Fig. 10b–d and Supplementary Video 7), as well as on sweaty skin after exercise (Supplementary Fig. 11). In addition, using the BIND connection, detection of EMG together with pressure and strain signals can also be achieved by another customized circuit (Supplementary Video 8
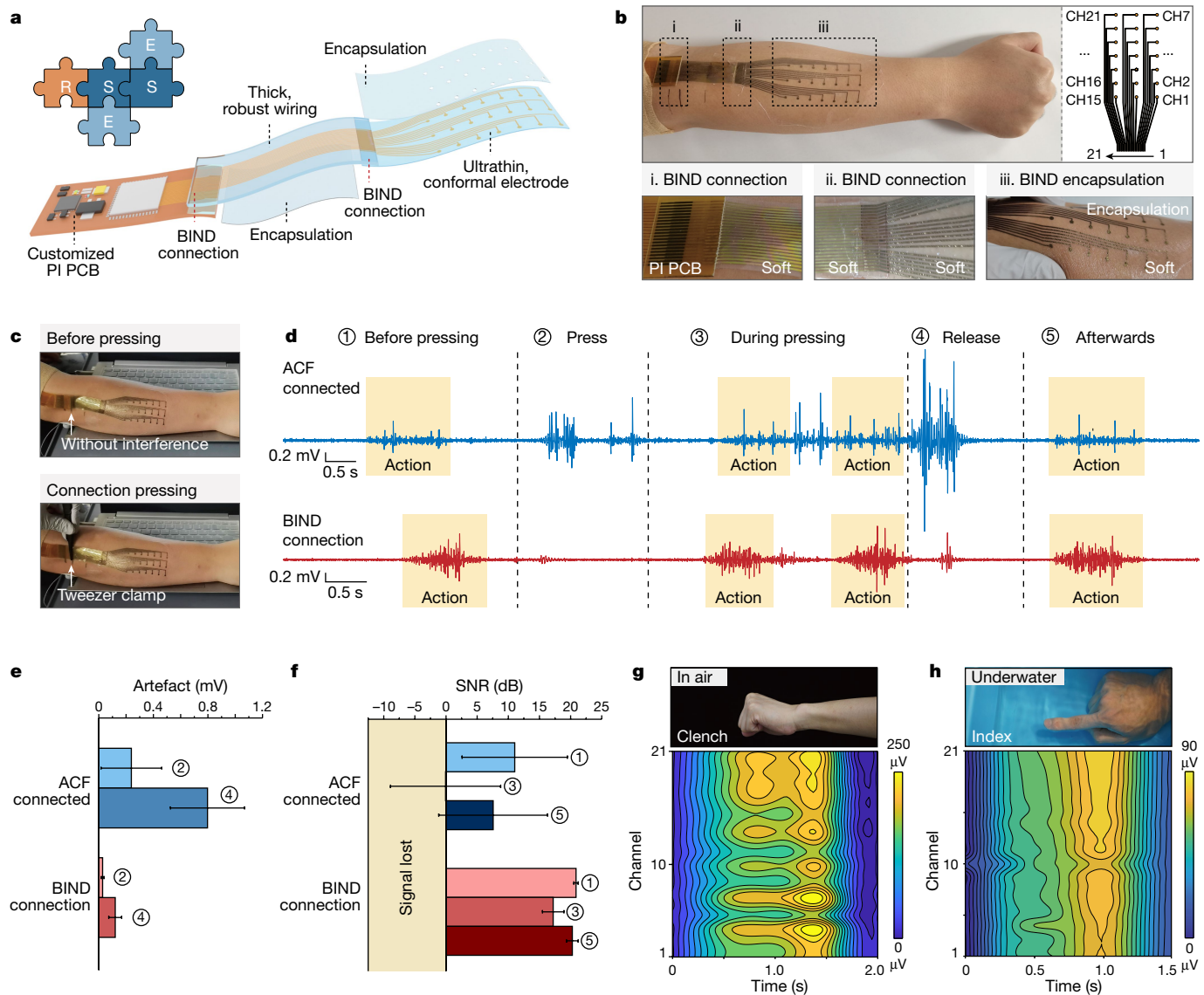
Fig. 4 | A 21-channel on-skin EMG electrode array assembled using plug-and-play BIND connections. a, Schematic of the EMG electrode array, in which the ultrathin electrode module, thick wiring module, PI PCB module and encapsulation modules are assembled through BIND connections. **b**, Photograph of an EMG electrode array on a human arm (top left) and the 21-channel electrode pattern (top right). Dotted boxes correspond to magnified view of flex–soft, soft–soft and soft–encapsulation BIND connections below. **c**, Photograph of a BIND connection before (top) and after (bottom) applying a tweezer clamp. **d**, Averaged EMG signal from 21 channels obtained from ACF-connected control electrode and BIND electrode when the connection between the wiring and PCB module is pressed and released. Circled numbers indicate different pressing stages. Yellow areas indicate action of fist clenching. **e**, Compared to control electrode, BIND electrode shows lower pressing (0.03 versus 0.24 mV) and releasing (0.12 versus 0.80 mV) artefact. **f**, SNR from the BIND electrode was largely maintained during (17.2 dB) and after (20.3 dB) pressing whereas control electrode suffered signal loss (−0.06 dB) during pressing and poor recovery (7.56 dB) afterwards. **g**,**h**, Photograph (top) and intensity contour mapping of 21-channel EMG signals (bottom) for the clench gesture in air (**g**), and index finger stretching underwater (**h**). Error bars in **e**,**f**, are s.d. from 21 channels. Circled numbers in **e**,**f** correspond to pressing stages in **d**.

and Supplementary Fig. 12). These experiments demonstrate that BIND connections can assemble various modules into complex stretchable devices in a plug-and-play manner, with high-quality signals and resistance to mechanical interferences.

Conclusion

In summary, we reported a highly stretchable BIND interface that can integrate soft, rigid and encapsulation modules together to form stretchable hybrid devices in a plug-and-play manner. Our BIND interfaces contain an interpenetrating metal and polymer nanostructure that forms continuous mechanical and electrical pathways, respectively.

The nanomechanics of the formation process was analysed by our biphasic network growth model. A soft–soft BIND connection with high electrical (>180%) and mechanical (>600%) stretchability was realized. The soft–rigid BIND connection involving rigid/flexible substrates such as PI, PET, glass and metal, also attained high electrical stretchability of roughly 200%. Further, soft–encapsulation BIND connections were highly adhesive, showing an interfacial toughness 60 times larger than conventional encapsulation. A stretchable hybrid device for in vivo neuromodulation assembled from modules with different form factors using BIND connections performed better than one-piece electrodes of a single thickness. We further showed that plug-and-play BIND connections used to build the more complicated 21-channel on-skin EMG

Article

electrode have enabled us to collect high-quality EMG signals, with resistance to mechanical interferences. With our plug-and-play BIND interface, building stretchable hybrid devices with different functionality and complexity is now simple and fast, offering infinite options for on-skin and implantable human–machine interaction.

Online content

Any methods, additional references, Nature Portfolio reporting summaries, source data, extended data, supplementary information, acknowledgements, peer review information; details of author contributions and competing interests; and statements of data and code availability are available at https://doi.org/10.1038/s41586-022-05579-z.

1. Squair, J. W. et al. Neuroprosthetic baroreflex controls haemodynamics after spinal cord injury. *Nature* **590**, 308–314 (2021).
2. Park, S. I. et al. Soft, stretchable, fully implantable miniaturized optoelectronic systems for wireless optogenetics. *Nat. Biotechnol.* **33**, 1280–1286 (2015).
3. Choi, S. et al. Highly conductive, stretchable and biocompatible Ag–Au core–sheath nanowire composite for wearable and implantable bioelectronics. *Nat. Nanotechnol.* **13**, 1048–1056 (2018).
4. Matsuhisa, N. et al. Printable elastic conductors by in situ formation of silver nanoparticles from silver flakes. *Nat. Mater.* **16**, 834–840 (2017).
5. Hua, Q. et al. Skin-inspired highly stretchable and conformable matrix networks for multifunctional sensing. *Nat. Commun.* **9**, 244 (2018).
6. Koh, A. et al. A soft, wearable microfluidic device for the capture, storage, and colorimetric sensing of sweat. *Sci. Transl Med.* **8**, 366ra165 (2016).
7. Kim, C.-C. et al. Highly stretchable, transparent ionic touch panel. *Science* **353**, 682–687 (2016).
8. Kim, D. C. et al. Material-based approaches for the fabrication of stretchable electronics. *Adv. Mater.* **32**, 1902743 (2020).
9. Boutry, C. M. et al. A hierarchically patterned, bioinspired e-skin able to detect the direction of applied pressure for robotics. *Sci. Robot.* **3**, eaau6914 (2018).
10. Shih, B. et al. Electronic skins and machine learning for intelligent soft robots. *Sci. Robot.* **5**, eaaz9239 (2020).
11. Huang, Z. et al. Three-dimensional integrated stretchable electronics. *Nat. Electron.* **1**, 473–480 (2018).
12. Valentine, A. D. et al. Hybrid 3D printing of soft electronics. *Adv. Mater.* **29**, 1703817 (2017).
13. Graudejus, O. et al. Encapsulating elastically stretchable neural interfaces: yield, resolution, and recording/stimulation of neural activity. *Adv. Funct. Mater.* **22**, 640–651 (2012).
14. Li, K. et al. A generic soft encapsulation strategy for stretchable electronics. *Adv. Funct. Mater.* **29**, 1806630 (2019).
15. Lu, N., Yoon, J. & Suo, Z. Delamination of stiff islands patterned on stretchable substrates. *Int. J. Mater. Res.* **98**, 717–722 (2007).
16. Niu, S. et al. A wireless body area sensor network based on stretchable passive tags. *Nat. Electron.* **2**, 361–368 (2019).
17. Graz, I. M. et al. Silicone substrate with in situ strain relief for stretchable thin-film transistors. *Appl. Phys. Lett.* **98**, 124101 (2011).
18. Fan, J. A. et al. Fractal design concepts for stretchable electronics. *Nat. Commun.* **5**, 3266 (2014).
19. Miyamoto, A. et al. Inflammation-free, gas-permeable, lightweight, stretchable on-skin electronics with nanomeshes. *Nat. Nanotechnol.* **12**, 907–913 (2017).
20. Sun, B. et al. Gas-permeable, multifunctional on-skin electronics based on laser-induced porous graphene and sugar-templated elastomer sponges. *Adv. Mater.* **30**, 1804327 (2018).
21. Gerratt, A. P. et al. Elastomeric electronic skin for prosthetic tactile sensation. *Adv. Funct. Mater.* **25**, 2287–2295 (2015).
22. Minev, I. R. et al. Electronic dura mater for long-term multimodal neural interfaces. *Science* **347**, 159 (2015).
23. Nair, V. et al. Laser writing of nitrogen-doped silicon carbide for biological modulation. *Sci. Adv.* **6**, eaaz2743 (2020).
24. Wang, W. et al. Strain-insensitive intrinsically stretchable transistors and circuits. *Nat. Electron.* **4**, 143–150 (2021).
25. Wang, S. et al. Skin electronics from scalable fabrication of an intrinsically stretchable transistor array. *Nature* **555**, 83–88 (2018).
26. Yoon, J. et al. Design and fabrication of novel stretchable device arrays on a deformable polymer substrate with embedded liquid-metal interconnections. *Adv. Mater.* **26**, 6580–6586 (2014).
27. Kang, J. et al. Modular and reconfigurable stretchable electronic systems. *Adv. Mater. Technol.* **4**, 1800417 (2019).
28. Tutika, R. et al. Self-healing liquid metal composite for reconfigurable and recyclable soft electronics. *Commun. Mater.* **2**, 64 (2021).
29. Dai, X. et al. Self-Healing, flexible, and tailorable triboelectric nanogenerators for self-powered sensors based on thermal effect of infrared radiation. *Adv. Funct. Mater.* **30**, 1910723 (2020).
30. Kadumudi, F. B. et al. The manufacture of unbreakable bionics via multifunctional and self-healing silk-graphene hydrogels. *Adv. Mater.* **33**, 2100047 (2021).
31. Son, D. et al. An integrated self-healable electronic skin system fabricated via dynamic reconstruction of a nanostructured conducting network. *Nat. Nanotechnol.* **13**, 1057–1065 (2018).
32. Hwang, H. et al. Stretchable anisotropic conductive film (S-ACF) for electrical interfacing in high-resolution stretchable circuits. *Sci. Adv.* **7**, eabh0171 (2021).
33. Chen, X. et al. Instant tough bioadhesive with triggerable benign detachment. *Proc. Natl Acad. Sci. USA* **117**, 15497 (2020). 27.
34. Yang, X. et al. Ultrathin, stretchable, and breathable epidermal electronics based on a facile bubble blowing method. *Adv. Electron. Mater.* **6**, 2000306 (2020).
35. Wang, T. et al. Mechanically durable memristor arrays based on a discrete structure design. *Adv. Mater.* **34**, 2106212 (2022).
36. Yan, X. et al. Quadruple H-bonding cross-linked supramolecular polymeric materials as substrates for stretchable, antitearing, and self-healable thin film electrodes. *J. Am. Chem. Soc.* **140**, 5280–5289 (2018).
37. Jeong, J.-W. et al. Materials and optimized designs for human-machine interfaces via epidermal electronics. *Adv. Mater.* **25**, 6839–6846 (2013).
38. Webb, R. C. et al. Ultrathin conformal devices for precise and continuous thermal characterization of human skin. *Nat. Mater.* **12**, 938–944 (2013).
39. Park, S. et al. Self-powered ultra-flexible electronics via nano-grating-patterned organic photovoltaics. *Nature* **561**, 516–521 (2018).

Methods

Preparation of BIND interface and connection

BIND interface. SEBS solution (Tuftec H1221, 13 wt.% in toluene) of 19 ml was poured into a glass mould with a lid (diameter 150 mm), and evaporated in a fume hood at room temperature for 3 days. The evaporation speed was controlled to be slow by opening a small slit for lid. The as-prepared SEBS film (thickness roughly 100 μm) was gently peeled off from the mould and fixed on supporting filter paper. The interpenetrating gold (or silver) nanoparticles were deposited using a tungsten boat (2.00 inches in diameter by 0.125 inches length, Kurt J. Lesker) and a vacuum thermal evaporator (Nano 36, Kurt J. Lesker, under a pressure of roughly 10^{-6} Torr, sample holder rotation 20%). A customized mask was used when needed.

As a control interface, PDMS–Au thin film was prepared by spin-coating PDMS precursor (SYLGARD 184, Dow Inc., curing ratio 10:1) on fluorinated Si/SiO$_x$ substrate at 600 rpm for 60 s, and was cured in a 60 °C oven for more than 12 h. Then Cr (5 nm, 0.5 Å s^{-1}) and Au (45 nm, 0.5 Å s^{-1}) was deposited on as-prepared PDMS film (thickness roughly 100 μm), using the same thermal evaporator parameters.

Soft–soft BIND connection. The BIND connection was obtained by pressing two BIND interfaces (5 mm width and 30 mm length) face-to-face, with an overlapping area of 5 mm (width) by 10 mm (length). The overlapping area was pressed with a 500 g weight for 1 h. For mechanical and electrical testing, the resistance measuring distance was 20 mm. As a control, a PDMS–Au connection was obtained by using sandwiched commercial conductive paste and tape of the same size to bind the PDMS–Au interface together. The commercial conductive pastes and tapes are: ACF tape (3M ECATT 9703), Cu tape (3M Scotch 77802), Carbon tape (PELCO Image Tabs) and four types of silver paste (MG Chemicals 8331, Electrolube fast silver paste, EPO-TEK H27D silver epoxy, EPO-TEK H20E silver epoxy).

Soft–rigid BIND connection. The rigid/flexible substrates (PI, PET, glass and metal) were coated with a self-assembled monolayer to enhance the adhesion with SEBS. The rigid/flexible substrates were treated with oxygen plasma to enhance hydrophilicity (Pico, Diener: pressure 5 mbar, power 80%, time 2 min), and immersed in trichloro(phenyl)silane solution (Sigma 440108, 0.1 vol.% in toluene) for 0.5 h, then rinsed with toluene, chloroform and ethanol in turn, before drying with nitrogen. Next, the rigid substrates were dip-coated with SEBS solution (13 wt.% in toluene), using scotch tape to define dip-coated area of roughly 6 mm length from the end. The rigid/flexible substrates with SEBS were put on a 60 °C hot plate in a fume hood for 0.5 h to evaporate the toluene. Then gold nanoparticles were deposited using thermal deposition, with the same parameters as before, resulting in rigid/flexible module with a BIND interface. To obtain a soft–rigid BIND connection, a rigid/flexible module with a BIND interface and another BIND interface were pressed together face-to-face, with an overlapping area of 5 mm (width) by 5 mm (length). The overlapping area was pressed using a 500 g weight for 1 h. For mechanical and electrical testing, the sample sizes were united to 5 mm (width) by 25 mm (length), and the resistance measuring distance was 15 mm. As a control, a PDMS–Au connection was synthesized, using sandwiched commercial conductive paste and tape to bind a Au-coated rigid/flexible substrate and PDMS–Au interface together, of the same size.

Soft–encapsulation BIND connection. For the peeling force test, the soft–encapsulation BIND connection was prepared by pressing an SEBS thin film (roughly 100 μm thickness) on a BIND interface, with 0.1 MPa of pressure for 1 h. A T-shaped 180° peeling test was applied (Extended Data Fig. 4f). Non-stretchable tapes were used as backing to avoid encapsulation or interface stretching. As a control, the PDMS–Au interface was covered with various encapsulation layers (thickness of roughly 100 μm). PDMS, polyurethane, Ecoflex10, Ecoflex20 and Ecoflex30 encapsulations were solvent cast on top of the PDMS–Au interface, whereas ACF tape and VHB tape encapsulations were directly pressed under 0.1 MPa pressure for 1 h.

For practical applications such as in vivo neuromodulation and the EMG electrode array, a much thinner encapsulation film was used (thickness of roughly 300 nm). Here the Si/SiO$_x$ wafer was treated with oxygen plasma to enhance hydrophilicity (pressure 5 mbar, power 80%, time 2 min), before spin-coating (600 rpm, 60 s) a water-soluble sacrificial layer (poly(4-styrenesulfonic acid) solution, Sigma 561223). Then dilute SEBS solution (3 wt.% in toluene, 2,000 rpm, 60 s) was spin coated, and toluene was evaporated in a fume hood slowly, resulting in a SEBS film of roughly 300 nm. The as-prepared sample was stuck to a PI frame and immersed in water to get a frame-supported SEBS encapsulation layer. To expose the region with a large area (line width roughly 5 mm), the encapsulation with the supporting layer was manually cut and then put on top of BIND interface before removal of the supporting layer. To expose the region with a medium area (line width 200 μm–5 mm), filter paper was cut into the shape of the exposed area using a laser engraving machine, then it was aligned and put on top of the BIND interface, before the ultrathin SEBS layer. By removing the sandwiched filter paper with sharp tweezers, the ultrathin encapsulation layer on top was removed together, resulting in a precise exposed area. For the exposed region with a small area (line width 100–200 μm), SU-8 pillars that had the same size of exposed area were fabricated using typical lithography and used as moulds. The water-soluble sacrificial layer and dilute SEBS were spin coated on top of the Si wafer with SU-8 pillars. After water immersion, a frame-supported encapsulation layer with holes was obtained, and then gently attached to the BIND interface with alignment.

Electrical, mechanical and electrochemical characterization

The electrical resistance was measured by semiconductor parameter analyser (Tektronix Keithly 4200-SCS, or Keysight 34450A), using liquid metal EGaIn (Sigma 495425) to make contact. To simultaneously obtain electrical and mechanical results, mechanical strain was applied by a mechanical tester (MTS Systems C42, or Thorlabs LTS150/M). The electrical performance was not stable in the first few stretching/releasing cycles due to microcrack propagation (Supplementary Fig. 2d), so all the electrical performance was measured after it reached stable status (usually after 100 cycles).

The sheet resistance was calculated by the resistance between opposite sides of a square-sized sample (0.5 cm^2). For surface sheet resistance, liquid metal was applied only on the surface of the sides. For cross-section sheet resistance, liquid metal was in contact with both the surface and cross-section of the sides. The sheet resistance measurement was conducted within 2 min to avoid the gap that may form between Au and EGaIn liquid metal after >1 h contact. The reaction between Au and EGaIn formed Au/Ga/In intermetallic compounds (for example, AuGa$_2$, AuGa, Au$_7$Ga$_3$, AuIn$_2$).

Electrochemical impedance was measured using an electrochemical workstation (Zahner Zennium), with a sample area of 0.5 cm (width) by 1.6 cm (length). The sample was immersed in PBS buffer solution, with Pt as a counter electrode and Ag/AgCl as a reference electrode.

AFM characterization

To prepare the cross-section, the BIND connection was cut with a glass blade using Leica EM UC7 Ultramicrotome, under an environment of −70 °C. For AFM imaging, height, adhesion and modulus mapping were measured using Bruker PeakForce QNM mode and current mapping was generated using Bruker PeakForce TUNA mode.

AES

AES measurement was performed on an Auger microprobe (JEOL JAMP-7830F). Both secondary electron imaging and AES were

Article

conducted with a primary electron beam with accelerating voltage of 10 keV and probe current of 10 nA. The analysis spot was roughly 10 μm in diameter and the sample was tilted at 30° throughout the analysis. For Auger depth profiling, floating micro-ion etching device generating an ion beam of 1 keV Ar$^+$ was used to sputter the sample across an area of 1.5 × 1.5 mm^2. Each cycle in the depth profiling recorded the spectra at an etching rate of 10 s per cycle. The spectral ranges for C KLL and Au MNN was 234–292 and 2,083–2,113 eV, respectively, collected with a step size of 1 eV and dwell time of 100 ms.

SEM imaging
SEM images were obtained using a JEOL JSM-7800FPRIME scanning electron microscope, at an acceleration voltage of 2–5 kV under secondary electron image mode.

Fabrication of the in vivo neuromodulation BIND device
The in vivo neuromodulation electrode consisted of an ultrathin and conformal electrode module with encapsulation, and a thick and robust wiring module with encapsulation. Each part was fabricated separately and assembled with a BIND connection (Supplementary Fig. 8).

Ultrathin, conformal electrode module with encapsulation. The water-soluble sacrificial layer and dilute SEBS solution was spin coated on a Si wafer to achieve an ultrathin SEBS substrate (thickness roughly 2–4 μm). Au nanoparticles (45 nm, 0.5 Å s^{-1}) were deposited using thermal evaporation. Then, filter paper-assisted encapsulation (thickness roughly 300 nm) was used to expose electrode pads. Finally, the whole module was stuck to a PI frame, and immersed in water before transferred to a flexible supporting paper.

Thick, robust wiring module with encapsulation. The thick, robust wiring was synthesized by depositing Au (45 nm, 0.5 Å s^{-1}) on SEBS film (roughly 150 μm), as described before. Then filter paper-assisted encapsulation (thickness roughly 300 nm) was used to expose the two ends.

As a control to show the advantages of modular design, two types of one-piece electrode were fabricated: an ultrathin electrode and a thick electrode. The two electrodes were fabricated by depositing Au (45 nm, 0.5 Å s^{-1}) on ultrathin SEBS film (roughly 2–4 μm) and thick SEBS film (roughly 150 μm), separately, by thermal evaporation as described before.

In vivo experiments
All in vivo experiments except bladder experiments were performed in Shenzhen Institutes of Advanced Technology, Chinese Academy of Sciences, which were approved and adhered to guidelines of its Institutional Animal Care and Use Committee (no. SIAT-IRB-180315-H0242). Sprague-Dawley rats (roughly 250–300 g) were anaesthetized by injecting sodium pentobarbitone (density 2%, dose 0.3 ml per 100 g) into the intraperitoneal space, and checked for the depth of anaesthesia. The body temperature was maintained at 37 °C using a heat pad.

Stimulation of sciatic nerve and peroneal nerve. In simultaneous CMAP stimulation and recording experiment, we used the BIND electrode to stimulate the peroneal nerve by a suture-free procedure (Supplementary Fig. 9). The biceps femoris was bisected to uncover and isolate the peroneal nerve, and the area was irrigated with sterile saline to ensure a clear view and good electrical contact. The ultrathin module of BIND electrode with supporting paper was first inserted into the gap in between nerve and underneath the muscle, then connected to the thick module. Next, the ultrathin module was wrapped around the nerve, and the tail was stuck with self-adhesion before removing the supporting paper. The stimulation pulse was applied using a Neurotrac electrical stimulator (monophasic pulse, width 150 μs, frequency 3 Hz), with 250 Ω of parallel resistance (Extended Data Fig. 8b). In a sciatic stimulation experiment, we used a BIND electrode to stimulate the

sciatic nerve with the same process as mentioned before. In the CMAP recording comparison experiment, we used a PI electrode to stimulate the peroneal nerve using a Neurotrac electrical stimulator (monophasic pulse, width 100 μs and frequency 1 Hz).

Subcutaneous CMAP recording on peroneus longus muscle. An incision was made on the skin for clear visualization, and the peroneus longus muscle was isolated with sterile saline irrigation. Similar to nerve stimulation, the BIND electrode was wrapped on the peroneus longus muscle using a suture-free wrapping procedure. In the CMAP recording comparison experiment, the control one-piece electrodes were wrapped around the peroneus longus muscle using the same procedure, and the reference electrode was placed on the rat's sole. In the CMAP simultaneous simulation and recording experiment, channels in the BIND electrode were used as both working and reference electrodes.

ECoG recording. The anaesthetized rat was positioned on a stereotaxic frame, then a longitudinal incision was performed to expose the skull surface and a round parietal craniotomy was made with a surgical drill. The BIND electrode was gently placed on the surface of cerebral cortex to record ECoG signals. The signal was relayed to external equipment (Bluetooth video electroencephalograph system, Nation Inc.). After half an hour of stable recording, penicillin (dose of 2 million units per kg of body weight) was injected to induce seizure, and the corresponding ECoG signal was recorded after about 0.5 h.

Bladder experiments. Bladder experiments were performed at the N.1 Institute of Health, Singapore, and animal care and use procedures were approved by the Institutional Animal Care and Use Committee of the National University of Singapore (R15-0592 protocol). The experimental subjects were adult female Sprague-Dawley rats (roughly 220–300 g), and were anaesthetized by injecting a mixture (0.2 ml per 100 g) of ketamine (37.5 mg ml^{-1}) and xylazine (5 mg ml^{-1}) into the intraperitoneal space for induction, and checked for the depth of anaesthesia regularly with supplementary dose of 0.1 ml per 100 g injected intraperitoneally for maintenance. After shaving hair on the lower abdominal area, incisions were made on the skin and underlying subcutaneous tissue, muscle and peritoneum using aseptic techniques. In the bladder stimulation experiment (Extended Data Fig. 8i,j), the BIND electrode was sutured on the bladder wall with the ultrathin part directly contacting the bladder wall. A catheter (C30PU-RCA1302, Instech Laboratories Inc.) was inserted into the bladder by a small cut at the bladder dome and secured with a 4-0 silk suture, which enabled injection of saline to fill the bladder and connection to an external pressure sensor (Transpac IV, ICU Medical Inc.). When electrical stimulation pulses (300 μs biphasic pulses, 10 Hz, 3 mA) were applied to the bladder wall by a BIND electrode for a duration of 5 s, the bladder muscle contracted and the external pressure sensor measured the increased intravesical pressure. In the bladder sensing experiment (Extended Data Fig. 8k), the BIND electrode was wrapped around the bladder wall. Normal saline was filled into bladder through the catheter and changes in bladder size were detected by BIND electrode.

Fabrication of 21-channel on-skin EMG BIND device
The 21-channel on-skin EMG BIND device consisted of the ultrathin, conformal electrode with encapsulation, the thick, robust wiring with encapsulation and the customized PI PCB. Each part was fabricated separately and assembled by the BIND connection in a plug-and-play manner (Supplementary Fig. 10 and Supplementary Video 4). For both the BIND electrode and ACF-connected electrode, the recorded signals were collected using the High-Performance and High-density Acquisition System of Neuromuscular Electrophysiological Signals (Model NES-64B01, SIAT, China), and applied to a 50 Hz notch filter and a 10 Hz high-pass filter, except that the signals under connection pressing and/

or stretching were applied to a 30 Hz high-pass filter. The on-skin experiments were performed in the Shenzhen Institutes of Advanced Technology, the Chinese Academy of Sciences (approved by the Shenzhen Institute of Advanced Technology Institutional Review Board, no. SIAT-IRB-180315-H0242) or in the School of Materials Science and Engineering, Nanyang Technological University Singapore (approved by its Institutional Review Board, no. IRB-2017-08-035).

Ultrathin, conformal electrode with encapsulation and thick, robust wiring with encapsulation. These two parts were synthesized using the same procedure as described in the section Fabrication of the in vivo neuromodulation BIND device, using a different customized mask for the 21-channel electrode pattern.

Customized PI PCB with BIND interface. The commercial customized PI PCB (17.5 µm of Cu on PI substrate, gold plating) was connected to the signal collector (Model NES-64B01, SIAT, China) by a cable socket. The exposed PI substrate at the end was coated with BIND interface, using the procedure described in the section Soft–rigid BIND connection.

As a control, the ACF-connected electrode used the same configuration, size and pattern as the BIND electrode. The ultrathin electrode was prepared by depositing Cr (5 nm, 0.5 Å s^{-1}) and Au (45 nm, 0.5 Å s^{-1}) on a PDMS substrate (thickness roughly 2–4 µm). The PDMS encapsulation layer was prepared by spin-coating diluted PDMS prepolymer (PDMS 10:1 curing ratio, 20 wt.% in hexane, 1,000 rpm, 300 s) on top of a fluorinated Si/SiO$_x$ substrate and cured in a 60 °C oven for more than 12 h. The PDMS encapsulation was applied with the filter paper-assisted method as described before. The thick, robust wiring with encapsulation was prepared on a PDMS substrate (thickness roughly 100 µm), using a similar procedure. Finally, commercial ACF tape was used to connect the ultrathin modules, the thick wiring modules and the customized PCB module together to obtain the ACF-connected electrode.

Data availability
The data supporting the findings of this study are available within the article and its Supplementary Information. Other raw data are available from the corresponding authors upon reasonable request. Source data are provided with this paper.

Author contributions Y.J. and Zhiyuan Liu conceived and coordinated the project and experiments. S.J. assisted the concept development, sample preparation and manuscript writing. J.S. prepared EMG electrodes and collected data in the EMG experiment. G.Z. and H.G. conducted the molecular dynamics in biphasic network growth model. T.S. conducted the Auger characterization and analysis. C.W. assisted the finite element analysis. W.L., H.J. and Zhihua Liu assisted flexible PCB design. M.Y. and Z. Lu assisted EMG electrode design. H.Z. assisted the EMG experiment. G.L. directed, and J.H., J.S. and Y.L. conducted the in vivo animal experiments except bladder. W.Y.X.P. and S.-C.Y. performed the in vivo bladder experiments. J.X., S.W., T.L. and X.Y. assisted BIND interface fabrication. Y.J. prepared all other samples, conducted all other experiments and wrote the manuscript. Z.B. and X.C. directed the project. All authors read and revised the manuscript.

Extended Data Fig. 1 | Electro-mechanical performance of soft modules connected by conventional pastes or BIND interfaces. a-d, Schematic (**a**) and photographs (**b-d**) of two soft PDMS/Au modules connected using commercial ACF. Stress concentration at connection region results in electrical failure at 50% strain (**b, c**) and mechanical failure at 76% strain (**d**). **e-h**, Schematic (**e**) and photographs (**f-h**) of two BIND interfaces connected without any pastes display conductivity up to 180% strain (**f, g**) and remain connected even at > 600% strain (**h**). **i**, Unlike connections using commercial pastes, BIND connection remained conductive (as shown by the low resistance change) even at 180% strain (left). Magnified graph of the low strain region (0–50%) on the right shows BIND connection experienced < 4 times change in relative resistance at 50% strain.
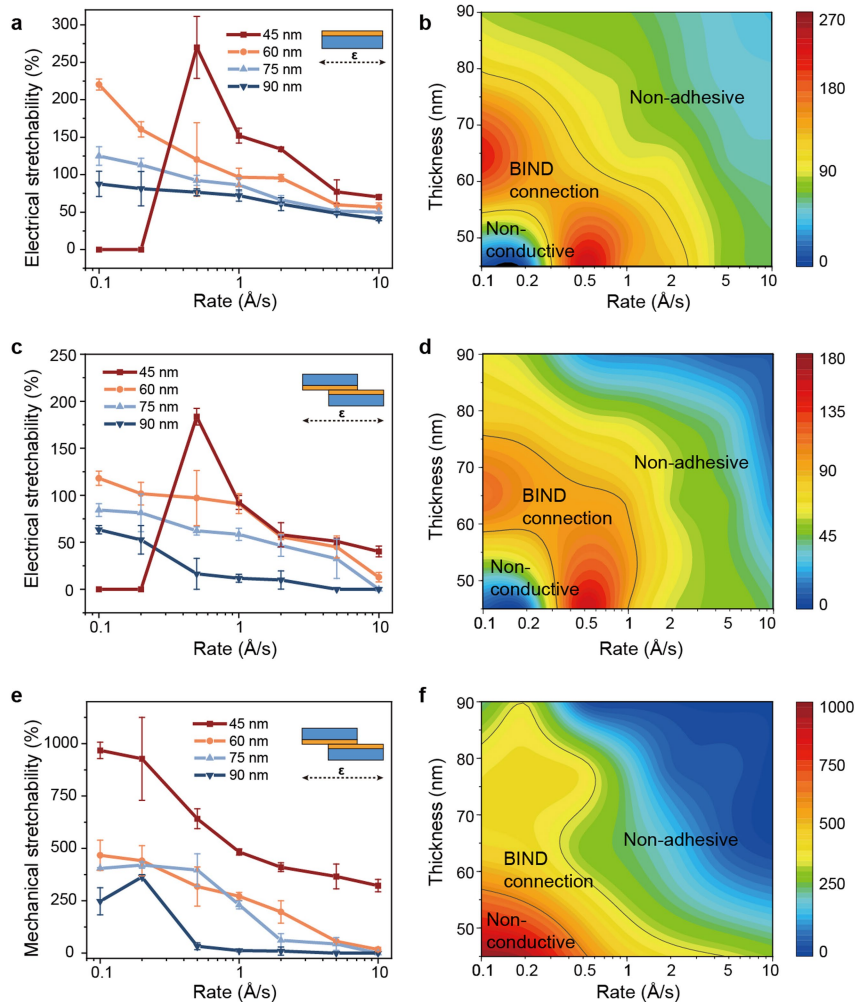
Extended Data Fig. 2 | Electro-mechanical performance of BIND interface depends on evaporation rate and thickness. a, b, Graph (**a**) and contour map (**b**) show the electrical stretchability of a single BIND interface as a function of evaporation rate and thickness. At the lowest evaporation rate (0.1–0.2 Å/s) and thickness (45 nm), a non-conductive interface is obtained. As evaporation rate or thickness increases, electrical stretchability peaks before decreasing to ~40%. **c, d,** Graph (**c**) and contour map (**d**) show the electrical stretchability of soft-soft BIND connection as a function of evaporation rate and thickness is similar to the single BIND interface in **a** and **b**. Only a limited combination of evaporation rate (0.5–1.0 Å/s) and thickness (45–60 nm) forms the BIND connection. Lower rates and thicknesses result in non-conductive connection while higher ones form non-adhesive interfaces. **e, f,** Graph (**e**) and contour map (**f**) show the mechanical stretchability of soft-soft BIND connection decreasing monotonically with increasing evaporation rate and thickness. Error bars in **a, c, e** are s.d. from 3–5 samples.

Article
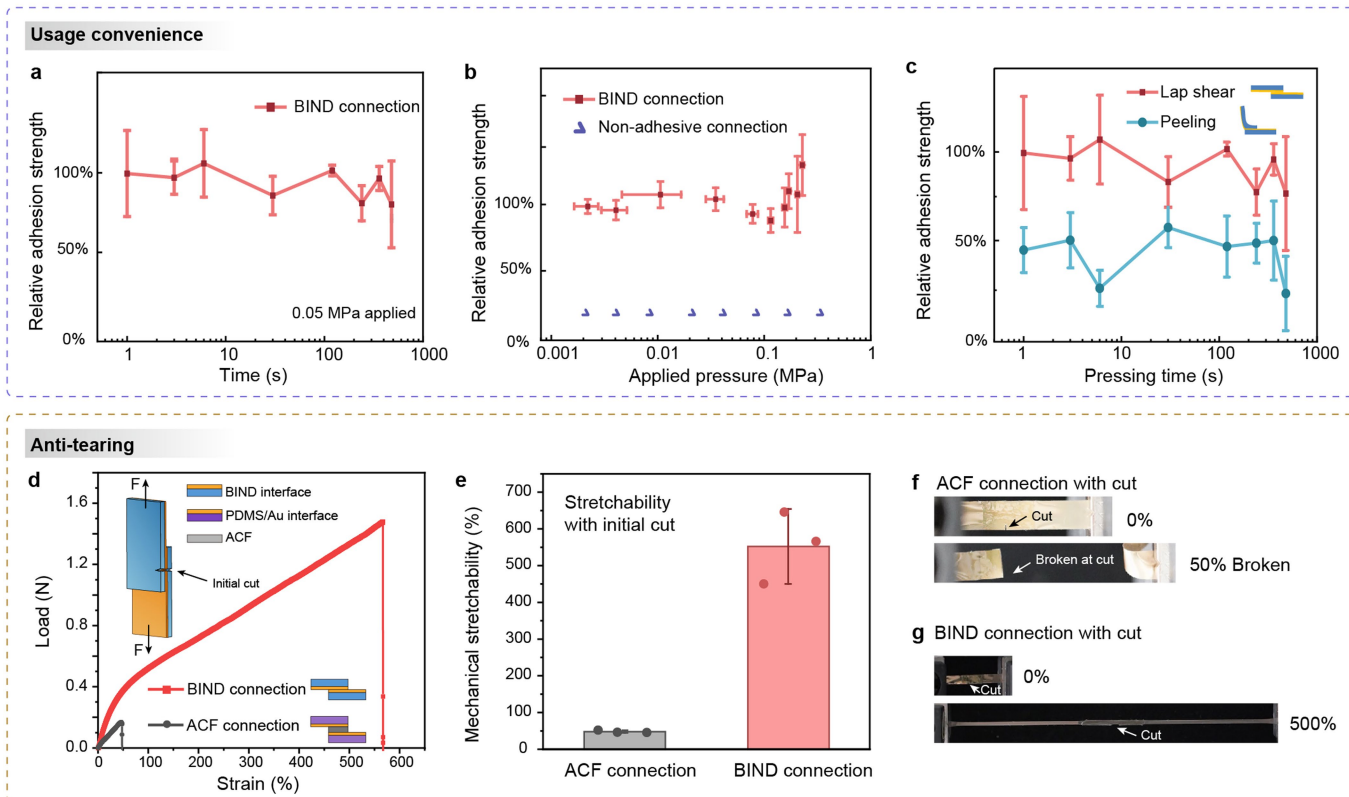
Extended Data Fig. 3 | Soft-soft BIND connection is easy to use and has anti-tearing properties. a-c, Pressing time (**a**), applied pressure (**b**) and peeling direction (**c**) do not influence the adhesion strength of BIND connection very much, indicating that BIND interfaces are easy to use. Simply pressing for 1 s at a low pressure of 0.001 MPa (*i.e.*, a normal finger press) is enough to connect BIND interfaces together. Consistent with the study in Extended Data Fig. 2, non-adhesive connections (120 nm thick Au layer) cannot adhere regardless of pressure. In all other characterization, lap shear test was employed because it's more common in practical application. **d-g**, Unlike ACF connection which breaks easily, BIND connection is resistant to cuts. Lap shear test on ACF and BIND connections that were initially cut (-1 mm) in the middle shows BIND connection withstood tearing forces >1.4 N (**d**) and remained stretchable even at > 500% strain (**e**). Photos show ACF connection with an initial cut broke easily at the cut location at 50% strain (**f**), while the initial cut in a BIND connection could still be stretched at 500% strain (**g**). Error bars in **a-c** are s.d. from 3-4 samples. Error bars in **e** are s.d. from 3 samples.
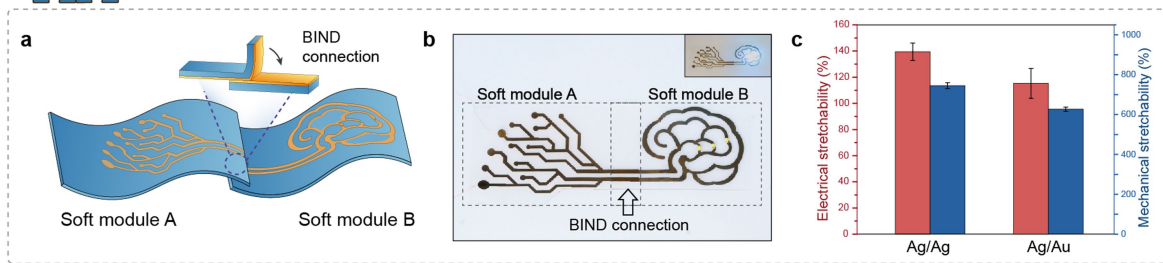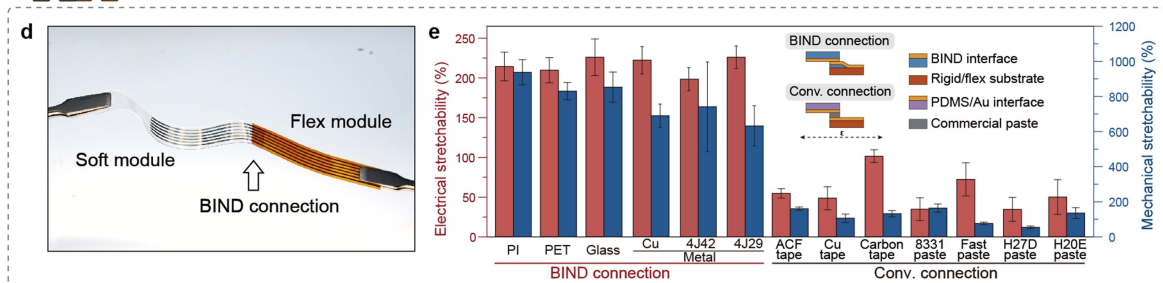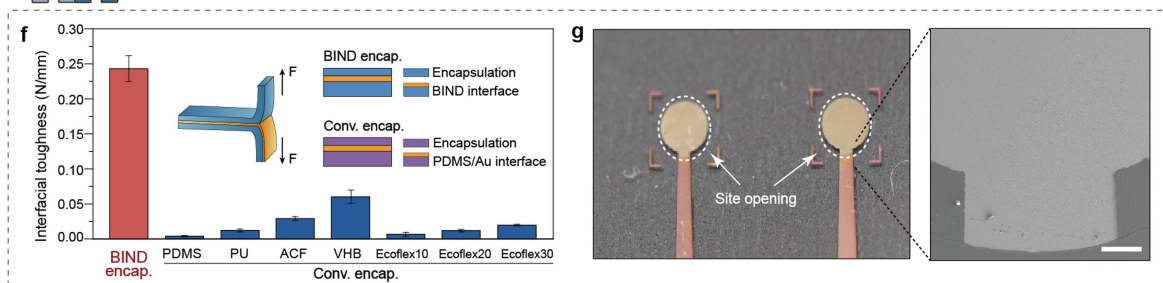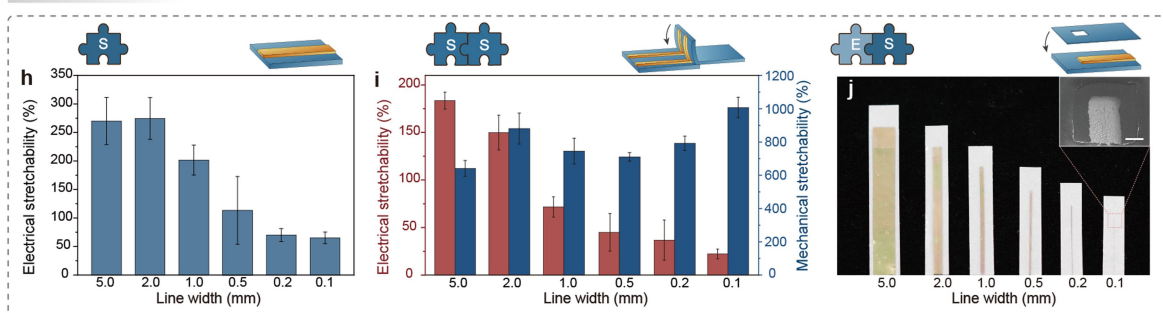
Extended Data Fig. 4 | Advantages of BIND connections. a, b, Schematic (**a**) and photo (**b**) showing two patterned BIND interfaces (on module A and B) are joined face-to-face via BIND connection. Inset in **b**: The BIND connection is electrically conductive to light an LED. **c,** BIND connections expanded to other conductive materials such as silver/silver and silver/gold connections also display robust electrical and mechanical stretchability. **d,** Photo of a soft module connected to a flexible PI module patterned with 6 electrode channels, via soft-rigid BIND connection. **e,** Soft-rigid BIND connection involving rigid or flexible substrates like PI, PET, glass, and metal show higher electrical (~200%) and mechanical (~800%) stretchability than conventional connection via various commercial pastes. **f,** Interfacial toughness of SEBS encapsulation layer on a

BIND interface (0.24 N/mm) is much larger than various other types of encapsulation layer bonded on a conventional PDMS/Au interface. All encapsulation layers are ~100 μm thick. **g,** SEM image of BIND encapsulation (~300 nm) on a pair of electrodes, exposing two pads for signal collection (SEM shown in magnified view). Scale bar in **g**: 100 μm. **h-j,** Resolution of single BIND interface, BIND connection, and BIND encapsulation can achieve 100 μm. The electrical stretchability of both BIND interface (**h**) and BIND connection (**i**) decreases with reduced line width, while the mechanical stretchability was kept relatively stable. The overall width was kept as 5 mm. Inset: SEM image of BIND encapsulation with exposed area of 100×100 μm^2. Scale bar: 50 μm. Error bars are s.d. from 3-4 samples.

Article
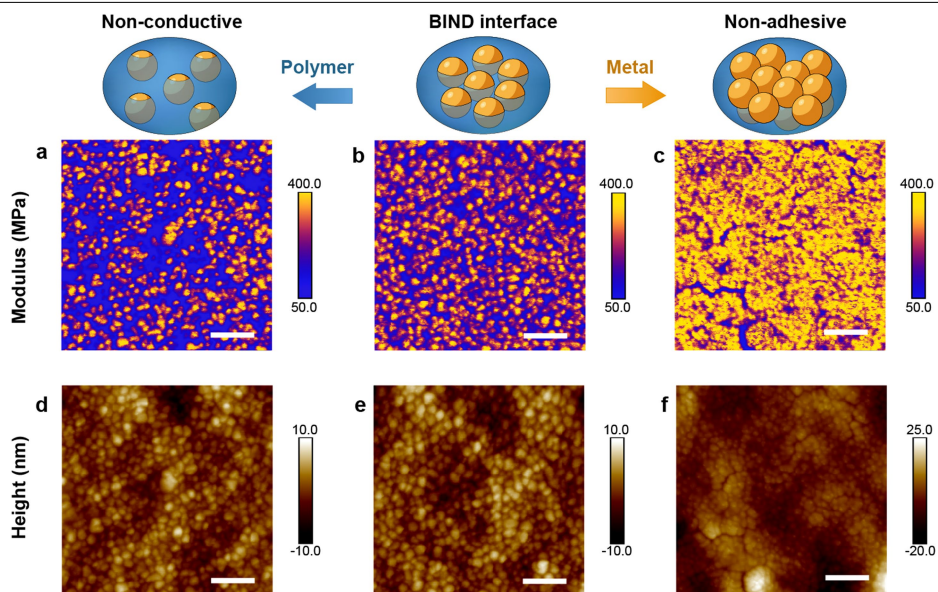
Extended Data Fig. 5 | Surface AFM mapping shows decreasing ratio of exposed polymer to metal phases, on non-conductive, BIND and non-adhesive interfaces. a-c, AFM modulus mapping show the polymer/metal ratio on the surface decreases from non-conductive interface (**a**), to BIND interface (**b**), to non-adhesive interface (**c**), which is consistent with the adhesion mapping (Fig. 2a). Due to the large modulus difference, polymer and metal phase can be easily distinguished and are labeled in blue and yellow color, respectively. **d-f**, AFM height mapping shows similar height variation on non-conductive interface (**d**) and BIND interface (**e**), because their height variation comes from the half-immersed gold nanoparticles. For non-adhesive interface (**f**), the height variation comes from the stacking gold nanoparticles on top of the polymer, so the variation range is slightly different from the non-conductive and BIND interfaces. Scale bar: 100 nm.
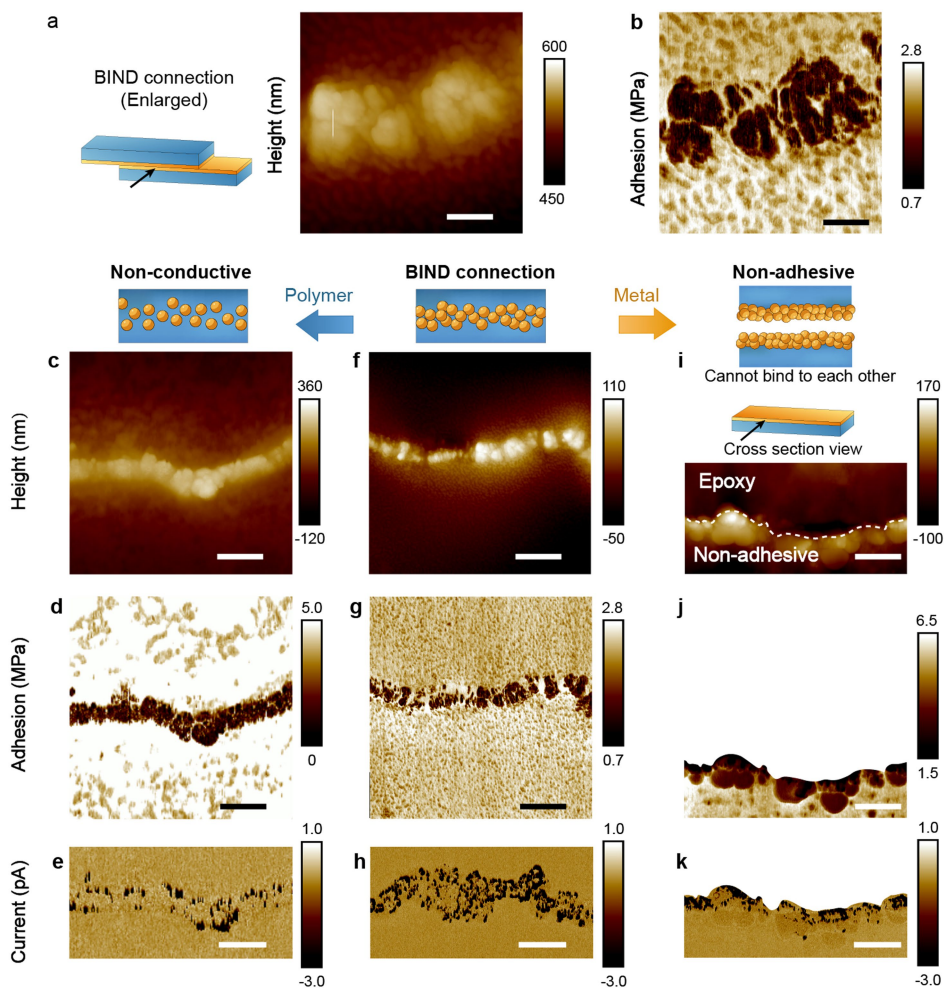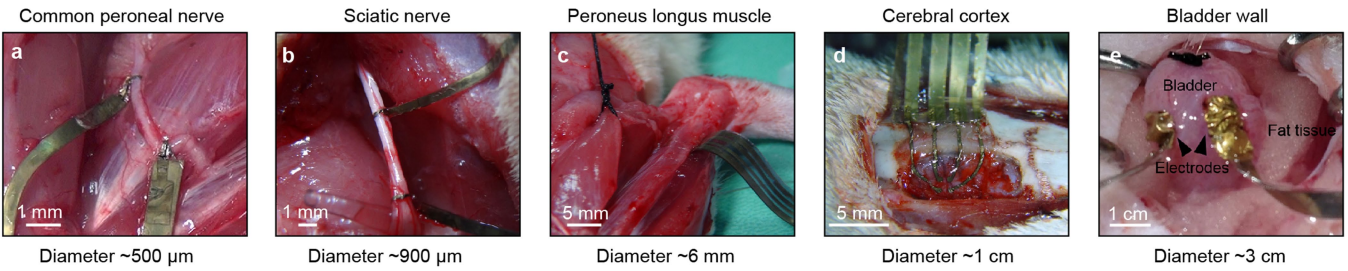
Extended Data Fig. 6 | Cross-sectional AFM mapping reveals decreasing penetrating Au nanoparticles inside non-conductive, BIND and non-adhesive interfaces. a, b, AFM height (**a**) and adhesion (**b**) mapping of a BIND connection show polymer and metal phases have an interpenetrating structure. Scale bar: 100 nm. **c-k**, AFM height, adhesion, and current mapping show that the non-conductive connection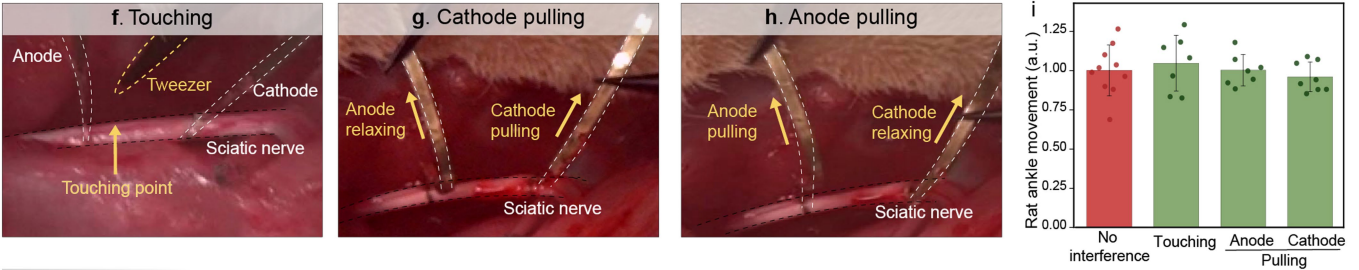 (**c-e**) has more interpenetrating Au nanoparticles than the BIND connection (**f-h**), while there is nearly no interpenetrating Au inside non-adhesive interface (**i-k**). Non-conductive connection and BIND connection were formed by pressing two interfaces together, while non-adhesive connection was formed by adhering epoxy to non-adhesive interface. White dash line in **i** shows the epoxy boundary, beyond which the epoxy region was removed for clearer view in **j-k**. Scale bar in **c-k**: 400 nm.
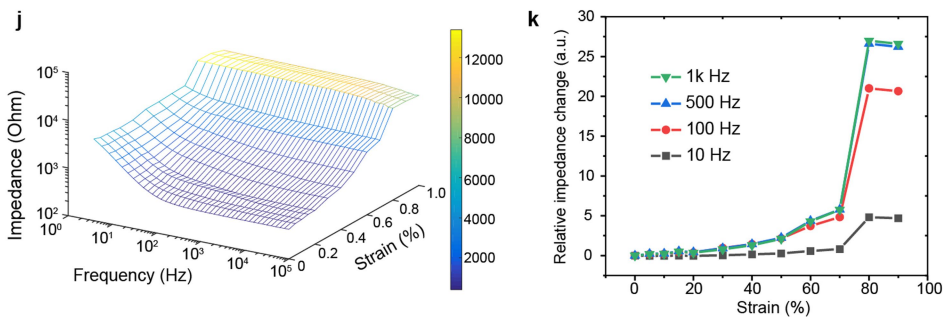
Conformal contact

Size increasing →

Common peroneal nerve

Diameter ~500 μm

Sciatic nerve

Diameter ~900 μm

Peroneus longus muscle

Diameter ~6 mm

Cerebral cortex

Diameter ~1 cm

Bladder wall

Diameter ~3 cm

Mechanical robustness

f. Touching

g. Cathode pulling

h. Anode pulling

i

Impedance

j

k

Extended Data Fig. 7 | *In vivo* neuromodulation BIND device is compatible with tissues of different sizes, with mechanical robustness against touching and pulling. a-e, BIND electrode conformally wraps around the common peroneal nerve (**a**), sciatic nerve (**b**) and *peroneus longus* muscle (**c**) without suturing. Conformal contact is also achieved when placed on the cerebral cortex (**d**), or sutured onto a bladder wall (**e**). The bladder experiment can be further improved in the future, to wrap the BIND electrode around the bladder to avoid suture. **f-i**, Mechanical interference such as touching (**f**), cathode pulling (**g**) and anode pulling (**h**) during sciatic nerve stimulation does not affect the stimulation performance very much. Here, the ultrathin part of the BIND electrode is wrapped around a sciatic nerve while the thick wiring part relays signals via a BIND connection. Stimulated effectiveness was measured by the moving distance of rat ankles upon applied interference (**i**). Error bars are s.d. from 7–10 movements. **j-k**, 3D map shows the impedance of BIND interface is typical of a metal-based stretchable electrode (**j**). Within the frequency range of interest (*e.g.*, ECoG 10-50 Hz, EMG 10-500 Hz), impedance remained low and nearly unchanged up to ~70% strain (**k**). Interfacial impedance of ultrathin electrode can be improved in the future by various methods (*e.g.*, coating the interface with low impedance materials such as PEDOT:PSS, or increasing the surface area). Because BIND connections construct electrical pathway by Ohmic contact between Au nanoparticles, its influence on impedance is the same as its electrical resistances in DC tests.
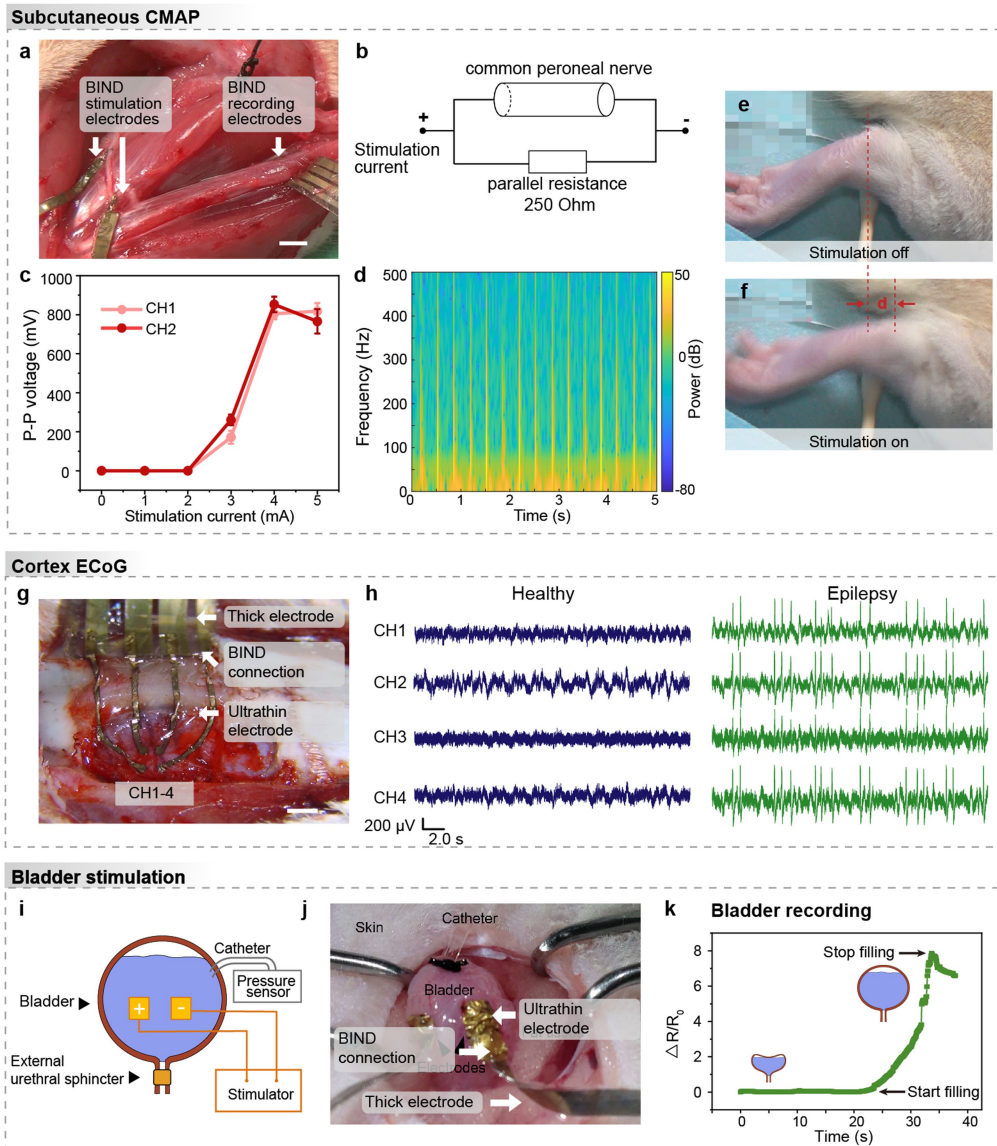
Extended Data Fig. 8 | The *in vivo* neuromodulation BIND electrode has various application, including subcutaneous CMAP, cortex ECoG, and bladder, demonstrating its usage universality. a-f, For simultaneous nerve stimulation and CMAP recording, one BIND electrode is wrapped around the common peroneal nerve and another is wrapped around the *peroneus longus* muscle (**a**). Stimulation current was applied to the common peroneal nerve with a parallel resistance of 250 Ω. (**b**). P-P voltage of CMAP is triggered when stimulation current reaches a threshold, then increases and plateaus (**c**). Spectroscopy of recorded CMAP shows obvious power density in the typical CMAP frequency range (10–500 Hz) (**d**). Ankle movement was measured by the distance, *d*, of rat ankle before (**e**) and during (**f**) stimulation. **g, h**, 4-channel BIND electrode on cerebral cortex for ECoG recording, consisting of ultrathin electrode module, and thick wiring module (**g**). ECoG signals of healthy and epilepsy rats differ in both amplitude and frequency (**h**). **i-k**, For bladder stimulation, two BIND electrodes were sutured onto the bladder wall to transmit electrical pulses, where the bladder contraction is recorded by external pressure sensor (**i, j**). For bladder recording, one BIND electrode is wrapped around the bladder. Normal saline is injected into the bladder through the catheter, and the corresponding expansion is detected by BIND electrode (**k**).

Article
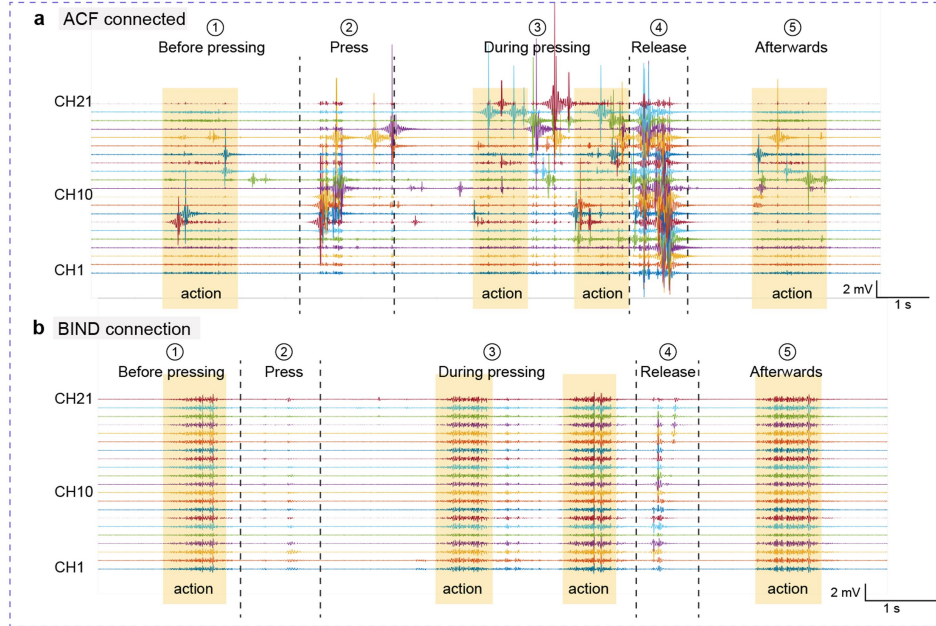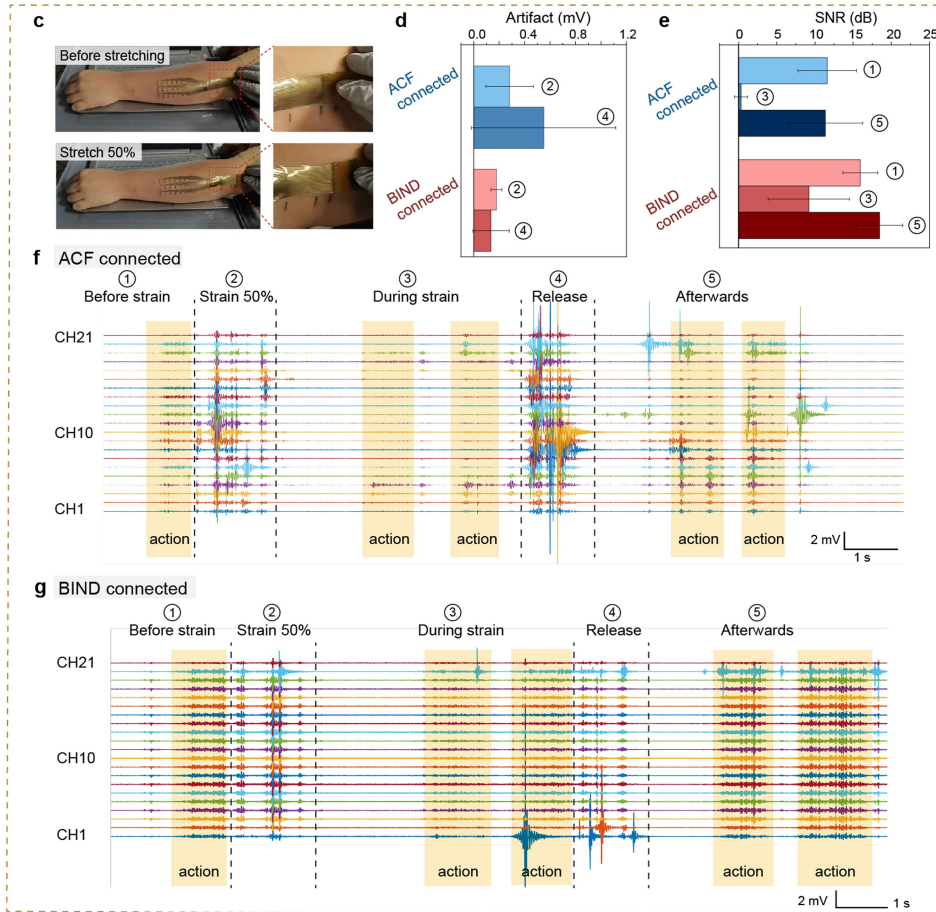
Extended Data Fig. 9 | See next page for caption.

Extended Data Fig. 9 | The 21-channel EMG electrode assembled via BIND connection shows high signal fidelity and resistance against mechanical interferences, including connection pressing and stretching (50%). **a-b**, EMG signals collected from ACF-connected control electrode (**a**) and BIND electrode (**b**) show that, pressing/releasing the connection between soft wiring and customized PCB induced noisy signals in control electrode, especially with actions. EMG signals from BIND electrode were less noisy and clearly distinguishable during and after pressure, indicating its resistance to pressure. **c-g**, Besides pressing, BIND connection also exhibits resistance to 50% stretching interference. One side of the BIND connection between soft wiring and customized PCB was fixed, and the other side was manually stretched to the 50% mark (**c**). Both electrodes showed noisy signals when stretched but the larger SNR in BIND electrode indicates that it can detect signals under strain (**d, e**). Releasing strain induced larger noise in control electrode but both electrodes recovered their ability to detect EMG signals after strain is released (**f, g**). All signals were subjected to a 50 Hz notch filter and a 30 Hz high-pass filter. Error bars in **d, e** are s.d. from 21 channels.
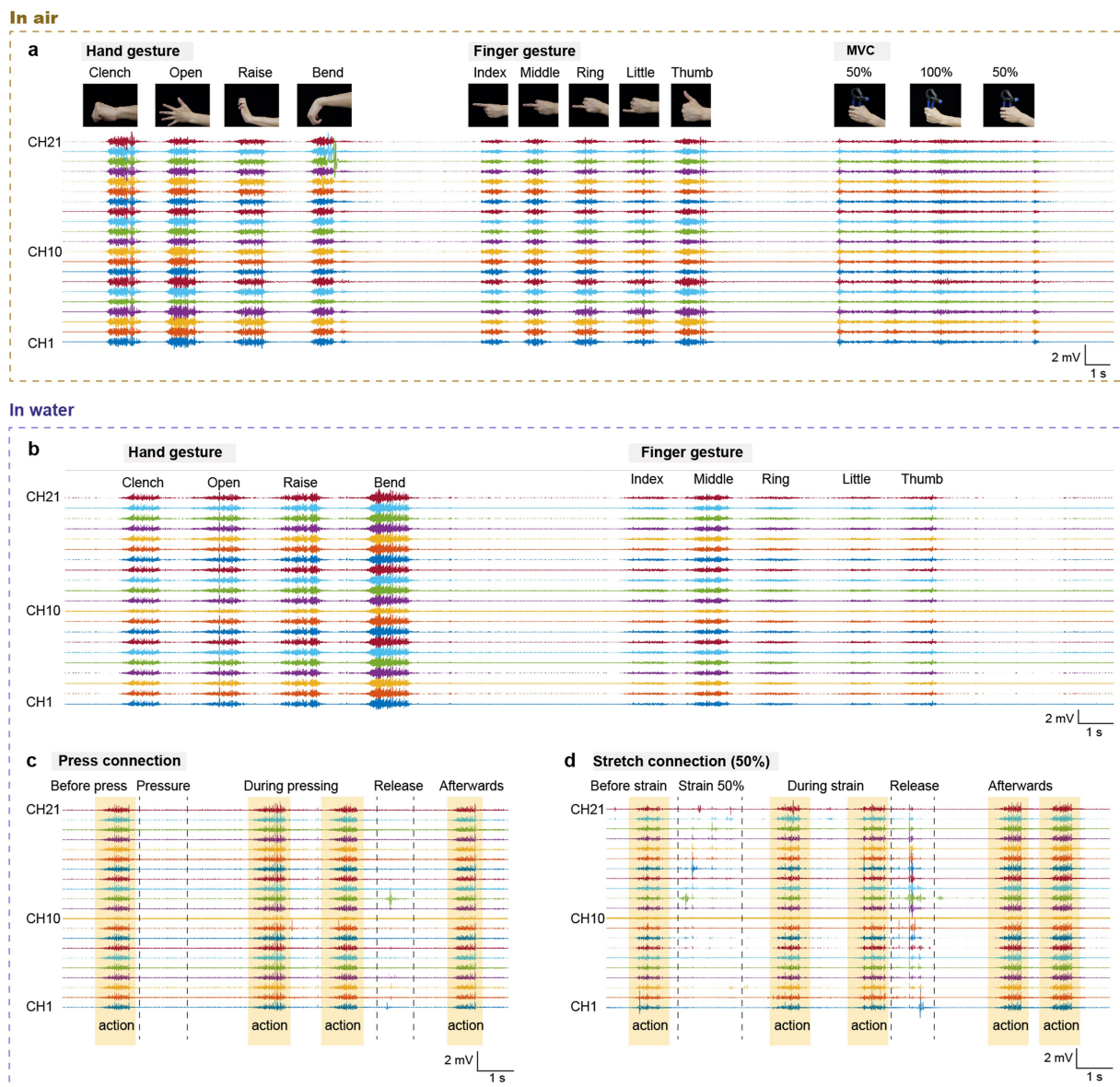
Extended Data Fig. 10 | 21-channel EMG electrode assembled via BIND connections maps various hand and finger gestures in air and underwater, with mechanical resistance to interference. a, BIND electrode detects EMG signals of hand gestures (clench, open, raise and bend), finger movements (stretching of individual fingers) and maximum voluntary contraction (MVC, measured by grip dynamometer) in air. **b-d**, Even underwater, BIND electrode detected EMG signals with high SNR from different hand and finger gestures (**b**) and tolerated pressure (**c**) and 50% strain (**d**) at connection points. High quality signals with little noise are seen before, during and after pressure or 50% strain. Here, the entire BIND electrode, including two BIND connections, was immersed in water. Signals in **a, b** were subjected to a 50 Hz notch filter and a 10 Hz high pass filter. Signals in **c, d** were subjected to a 50 Hz notch filter and a 30 Hz high pass filter.